Supporting Information

2D $TaSe_2$ as a Zero-Strain and High-Performance Anode Material for Li^+ Storage

Fei Wang, Jian Mao*.

*Corresponding author: Prof. Jian Mao, E-mail: maojian@scu.edu.cn.

College of Materials Science and Engineering, Sichuan University, Chengdu 610065, China.

Methods

Exfoliation of 2D $TaSe_2$

0.1 g Bulk $TaSe_2$ powder was added to 10 mL ethanol, and the mixture was sonicated for 15 h. The upper suspension was centrifuged and dried (70 ℃, 10 h) in the vacuum condition to obtain the 2D $TaSe_2$.

Characterizations

The morphology and structures were tested by SEM (JSM-7500F), TEM (JEM-2100F) and AC-STEM (Titan Themis Z). The XRD patterns and XPS spectra were collected by powder diffractometer (EMPYREAN) and X-ray photoelectron spectrometer (XSAM800). The *in-situ* XRD data were obtained using a Bruker D2 powder diffractometer. The specific surface area was tested by a specific surface and porosity analyzer (ASAP2460). The thickness of 2D $TaSe_2$ was tested on AFM (Bruker Dimension Icon). The conductivity of electrodes with diameters of 14.2 mm and

scraped slurry thickness of 50 μm was tested by BM901 multimeter. For the testing of conductivity, 20 parallel tests were conducted and the average value is calculated.

The active materials (2D and bulk $TaSe_2$) were mixed with polyvinylidene fluoride in N-methyl-2-pyrrolidinone solvent (mass ratio of 95:5 wt%) without adding conductive additive due to the excellent conductivity of $TaSe_2$. The slurry was scraped onto the copper foil to prepare the electrodes. 2032 Coin-type cells were assembled in an argon glove box. The loading mass of active material is around 3 mg (half cells) except for special instructions. At least five cells were used to confirm reproducibility.

The rate and cycling performance were tested using a LAND tester by the galvanostatic method. The EIS and CV were performed by a CHI660E electrochemical workstation. The frequency of 100 kHz to 10 Hz and AC perturbation of 5 mV were set in EIS tests. For the GITT measurement, the current pulse of 0.2 A g^{-1} was applied for 270 s while the following relaxation time is 1080 s. The electrochemical properties are tested at room temperature. For the *in-situ XRD* tests, the current density is as low as 0.05A/g and the scanning rate is 5 degree/min.

DFT Simulations

The spin-polarized DFT calculations were conducted with the Cambridge sequential total energy package (CASTEP) using the Perdew–Burke–Ernzerhof (PBE) generalized gradient approximation (GGA) functional. The convergence criteria (energy cutoff of 500 eV, total energy tolerance of 2 × 10-5 eV and force difference of 0.05 eV/ Å) were set. The van der Waals (vdW) force was corrected by the TS's method. For calculating band structures, 12*12*5 grid k-points were used, if not 5*5*2 grid k-points were used.

The linear synchronous transition/quadratic synchronous transit (LST/QST) tools were employed to calculate the diffusion energy barrier.

Determination of Li^+ diffusion energy barrier using the LST/QST tools in the CASTEP code

The simplest way to calculate a reaction/diffusion path is to start at a saddle point and take successive steps in the direction of the negative gradient. This steepest descent approach leads to a minimum energy path (MEP). If the coordinate system is mass-weighted, this is called an intrinsic reaction coordinate (IRC). The DMol[3] uses the nudged elastic band (NEB) method for minimum energy path calculations. The NEB method introduces a fictitious spring force that connects neighbouring points on the path to ensure continuity of the path and projection of the force so that the system converges to the MEP. The NEB method has been used widely in the study of solid-state physics and molecules. The advantage of the NEB algorithm is that it provides a fast qualitative examination of the MEP. The LST/QST tools are widely used to explore the energy barrier for the diffusion of ions/atoms. [1, 2]

Used separator and electrolyte

Celgard 2500 (polypropylene) was used as the separator. For the electrolyte, 1M $LiPF_6$ was dissolved into the mixture of ethylene carbonate (EC), dimethyl carbonate (DMC) and ethyl methyl carbonate (EMC) with the volume ratio of 1:1:1.

Calculation of charge density difference

The charge density difference ($\triangle\rho$) is calculated from the following expression.

$$\triangle \rho = \rho_t - \sum \rho_i \quad \text{(S1)}$$

where the ρ_t is the electron density of the total system and the $\sum \rho_i$ is the electron density summation of all atoms.

Calculation of volume expansion

Because lattice parameters of a and b are not change, the volume expansion (△V) is calculated by the following Equation.

$$\triangle V = \triangle c \tag{S2}$$

Where the △c are the change of lattice parameters along c axis, which can be calculated by Bragg equation based on the XRD patterns.

Calculation of lithiated chemical formula by specific capacity

The number of Li^+ (n) at full lithiation can be calculated by the following equation.

$$n = \frac{3.6MC}{F} \tag{S3}$$

where the M, C and F are the molecular weight of $TaSe_2$, the specific capacity of bulk/2D $TaSe_2$ and the Faraday constant, respectively. The specific capacity of bulk/2D $TaSe_2$ is considered 800 and 320 mAh g^{-1} for 2D and bulk $TaSe_2$, which are obtained at 0.1 A g^{-1}.

Calculation of capacity distribution

The contributions of diffusion-controlled insertion process and the surface-controlled pseudocapacitive behaviour can be evaluated by the power-law relationship given by Eq. S4.

$$i = av^b \tag{S4}$$

where *i* is the peak current, υ is the scan rate, and a/b are the adjustable parameters. The b values can be obtained from the slope of the log(*i*) - log(υ) plots. b=0.5 implies that the current is limited by the diffusion-controlled insertion process, and b=1 is

equivalent to the surface-controlled perfect pseudocapacitive behaviour.

To quantity the individual contribution of diffusion-controlled and pseudocapacitive behaviours to the total Li^+ storage, the Eq. S5 is used.

$$i(\upsilon) = k_1\upsilon + k_2\upsilon^{1/2} \tag{S5}$$

where $i(\upsilon)$, $k_1\upsilon$ and $k_2\upsilon^{1/2}$ represent the total current, surface-controlled current and diffusion-controlled current, respectively. The constants, K_1 and K_2, are determined by the $(i/\upsilon^{1/2})$ - $\upsilon^{1/2}$ curve.

Calculation of Li^+ diffusion coefficient by GITT curve

$$D = \frac{4}{\pi\tau}(\frac{m_B V_M}{M_B S})^2(\frac{E_s}{E_t})^2 \tag{S6}$$

Where the D is diffusion coefficiency; the m_B and M_B are the active mass and molar mass of the electrodes, respectively; the V_M is the molar volume; and the S is the active surface area of the electrodes.

Calculation of adsorption energy:

The adsorption energy (E_{ad}) is calculated by Eq. S7.

$$E_{ad} = E_{bulk+Li} - E_{bulk} - E_{Li} \tag{S7}$$

where $E_{bulk+Li}$, E_{bulk} and E_{Li} are the energy of a Li^+ in hosts, hosts and a Li^+.

Calculation of open circuit voltage

The ion insertion potential is calculated using the following open circuit voltage (OCV) equation. [3]

$$OCV = -\frac{E_{Lix_2TaSe_2} - E_{Lix_1TaSe_2} - (x_2 - x_1) - E_{Li}}{x_2 - x_1} \tag{S8}$$

where $E_{Lix2TaSe2}$ is the total energy of the 2D/bulk $TaSe_2$ adsorbing Li atoms, x_2 and x_1 are the two adjacent concentrations of absorbed Li^+ on the 2D/bulk $TaSe_2$, and E_{Li} represents the energy per Li atom in the bcc lattice.

Calculation of specific capacity retention (SCT) value:

Based on Figure 3(a), the SCT values are calculated by Eq. S9.

$$SCT = \frac{C_x}{C_{0.2}} \times 100\% \tag{S9}$$

where, $C_{0.2}$ and C_x represent the average specific capacities at current densities of 0.2 and x A/g, respectively.

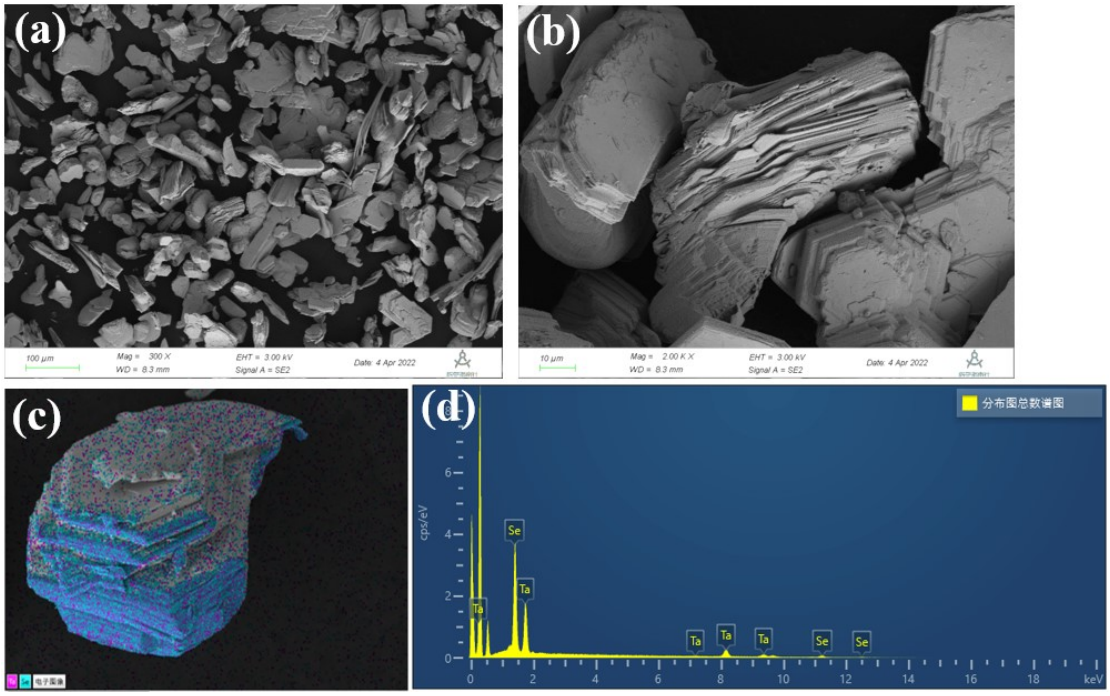

Figure S1. **(a)-(b)** SEM morphology of bulk $TaSe_2$. **(c)-(d)** EDS tests of bulk $TaSe_2$.

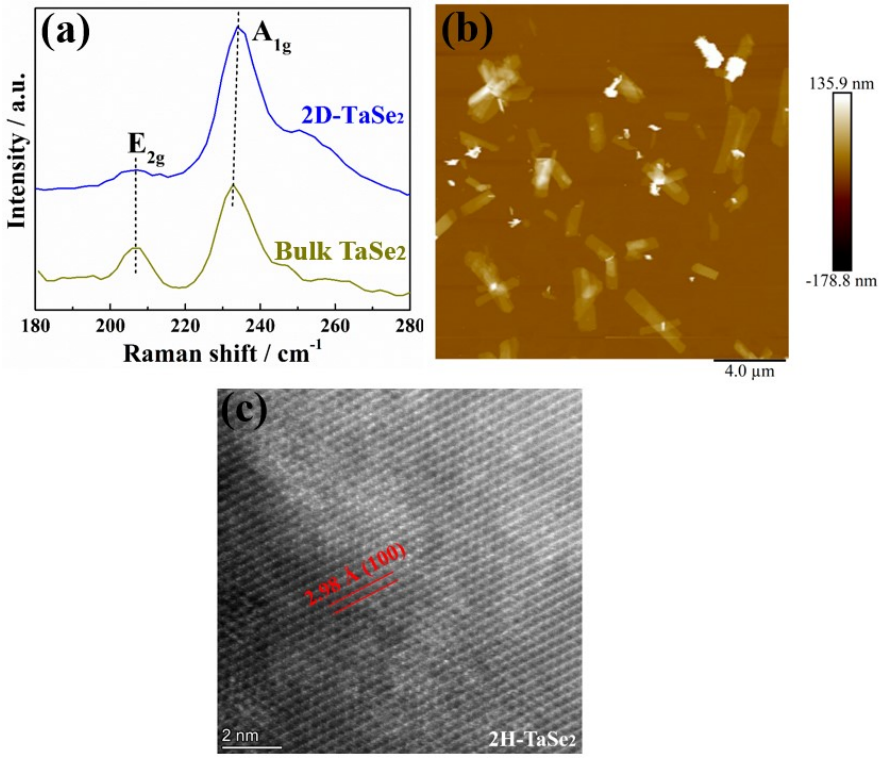

Figure S2. **(a)** Raman spectra of 2D $TaSe_2$ and bulk $TaSe_2$. **(b)** AFM image with a large number of 2D $TaSe_2$. **(c)** HR-TEM morphology of bulk $TaSe_2$.

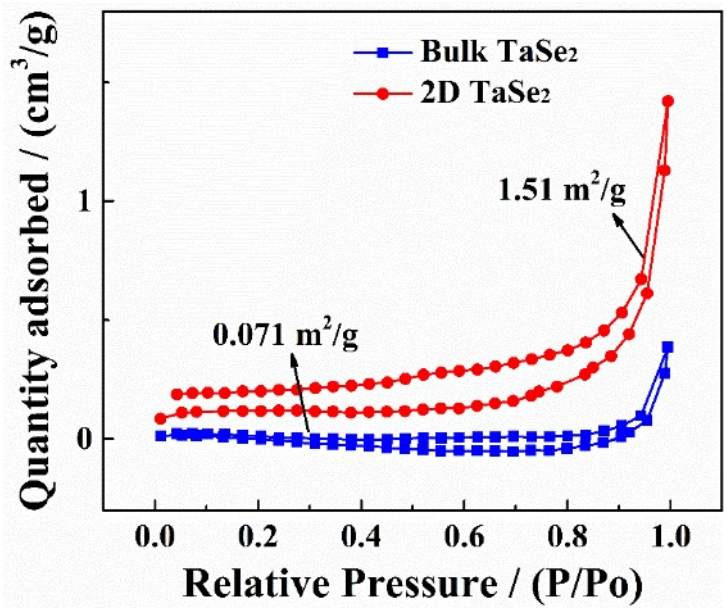

Figure S3. N_2 adsorption/desorption isotherms of bulk $TaSe_2$ and 2D $TaSe_2$.

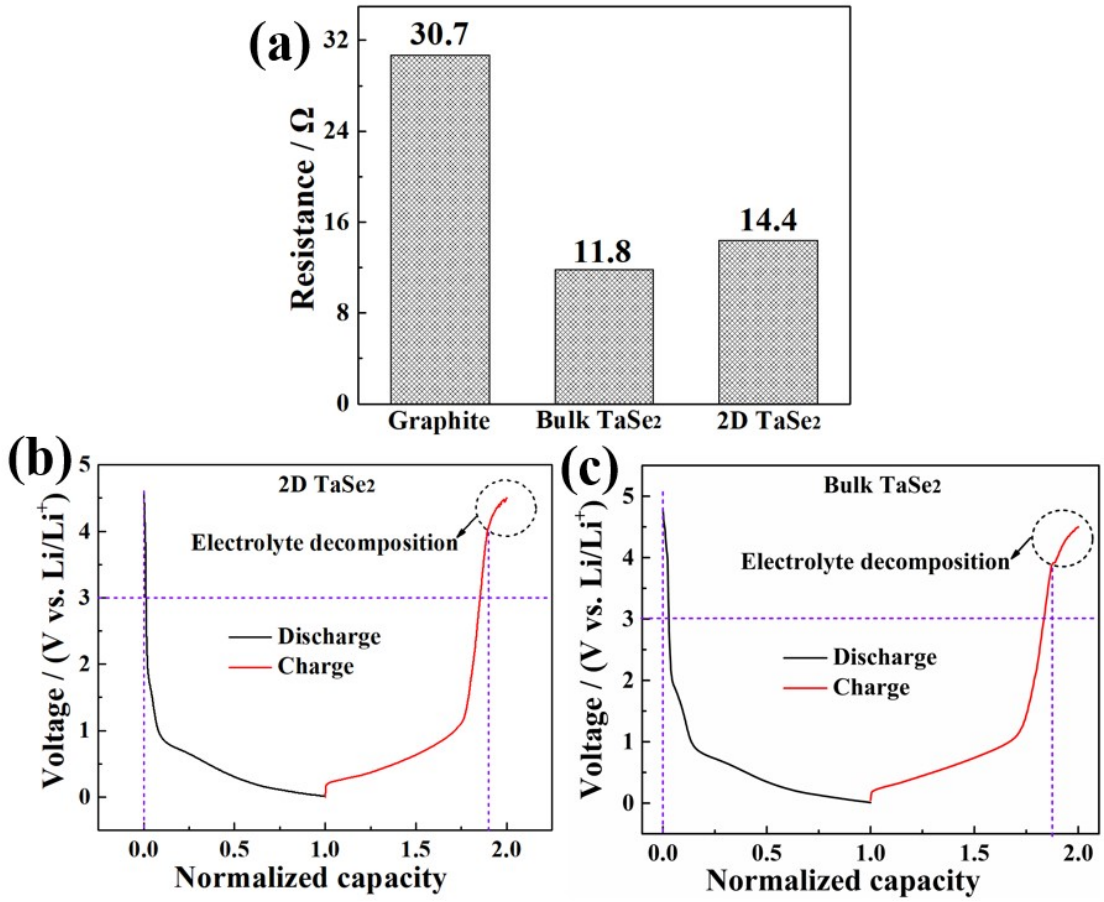

Figure S4. **(a)** Resistances of 2D $TaSe_2$, bulk $TaSe_2$ and graphite electrodes. Dischrage-charge curves of **(b)** 2D and **(c)** bulk $TaSe_2$ between 0.01-4.5 V.

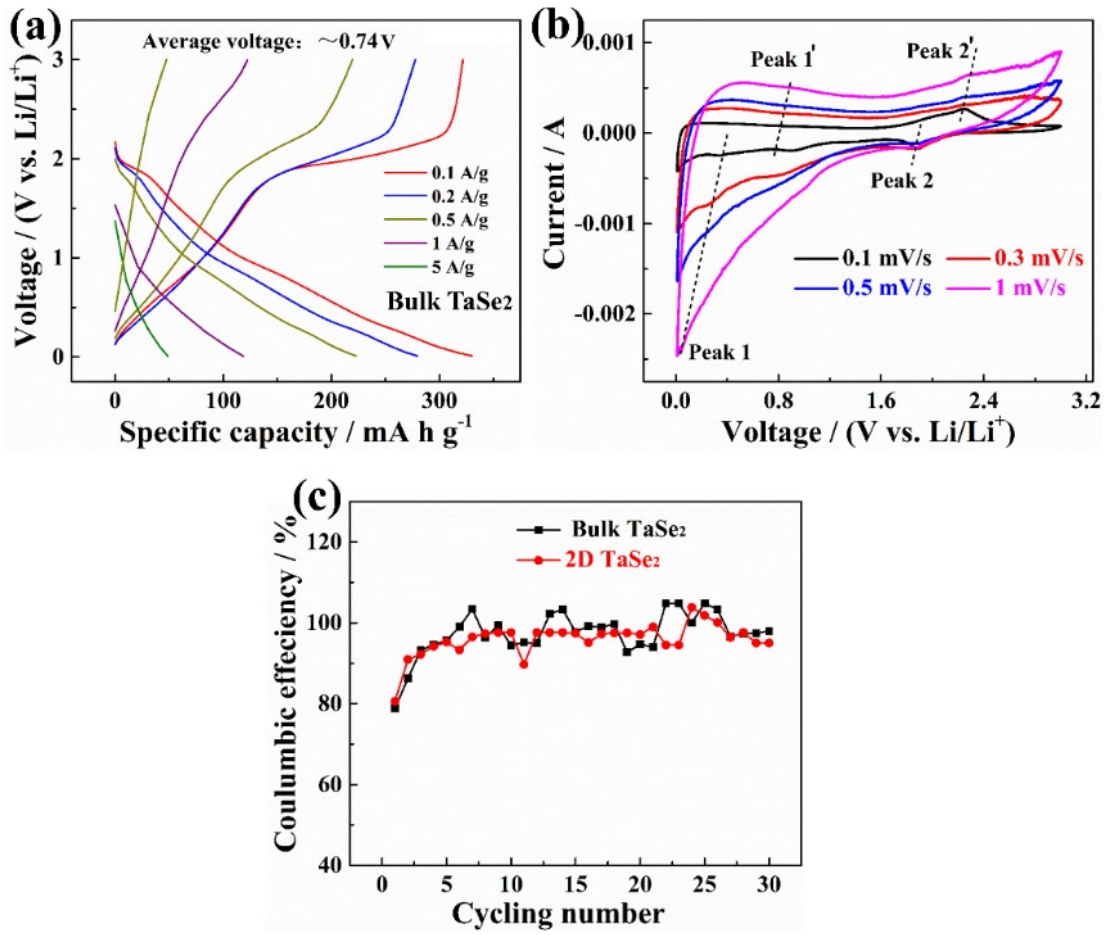

Figure S5. **(a)** Discharge-charge curves of bulk $TaSe_2$. **(b)** CV curves of bulk $TaSe_2$ with various scanning rates. **(c)** Coulombic efficiency of bulk and 2D $TaSe_2$ in rate-performance tests.

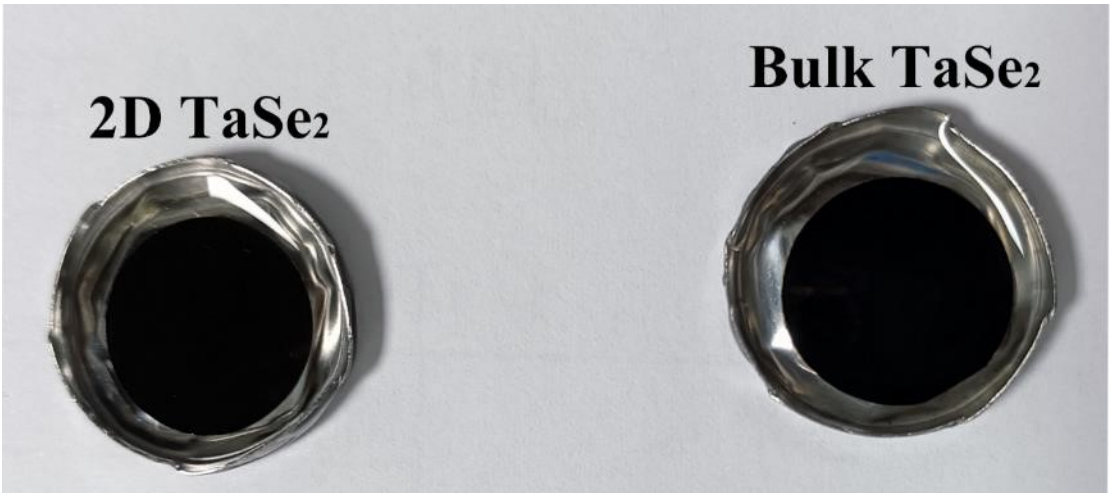

Figure S6. Morphology of 2D/bulk $TaSe_2$ anodes after cycling.

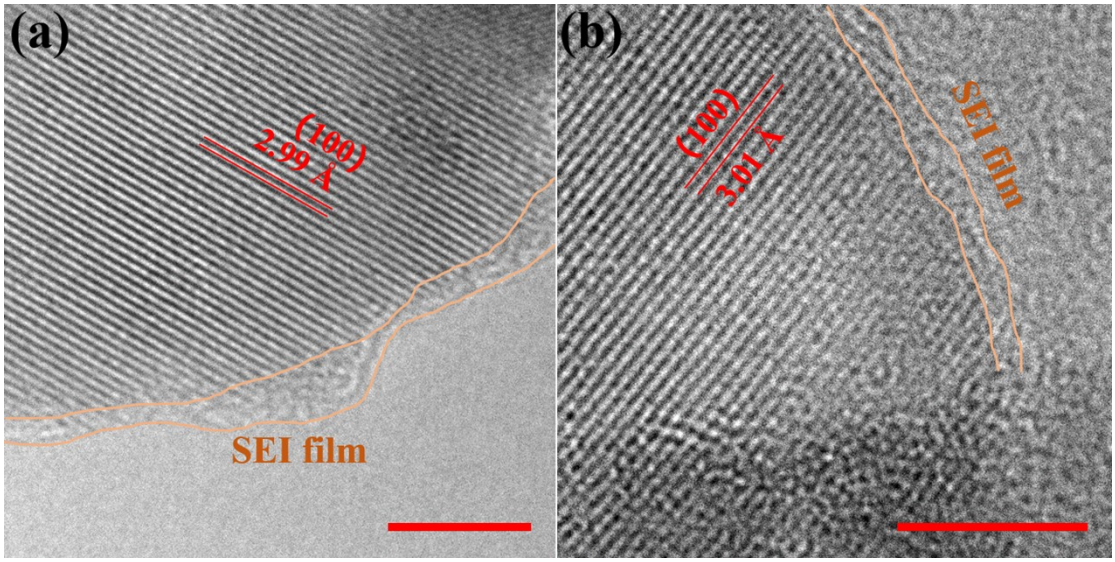

Figure S7. After 2000 cycles, the TEM morphology of (a) 2D $TaSe_2$ and (b) bulk $TaSe_2$ at 0.01 V (the scale bar: 5 nm).

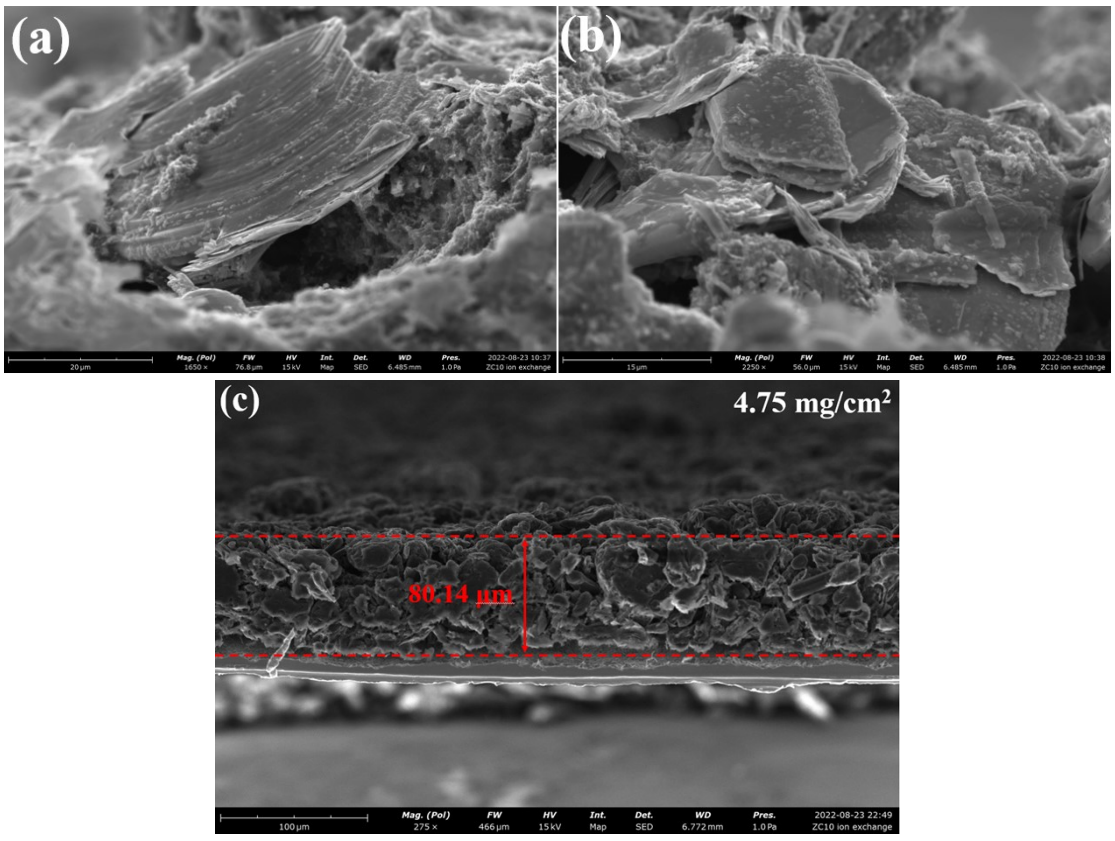

Figure S8. Morphology of **(a)** bulk and **(b)** 2D $TaSe_2$ materials after 2000 cycles. **(c)** Cross-section morphology of graphite electrode with loading mass of 4.75 mg cm^{-2}.

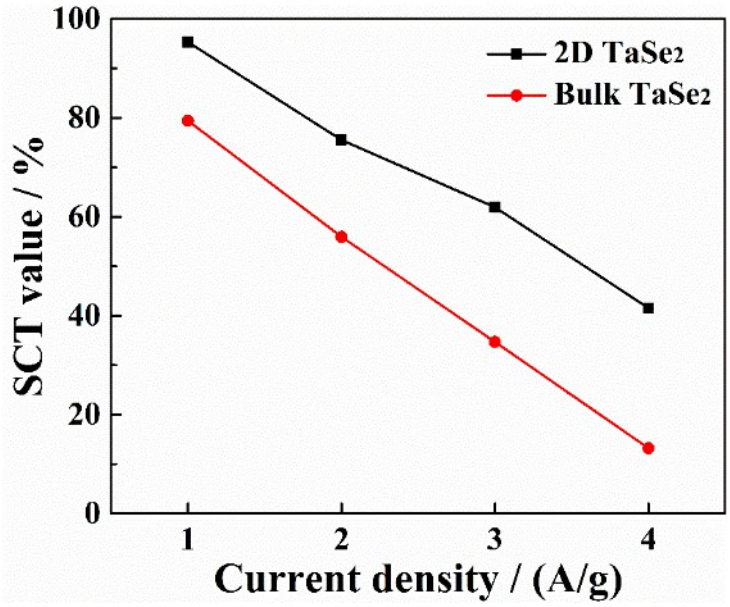

Figure S9. specific capacity retention (SCT) of the two electrodes.

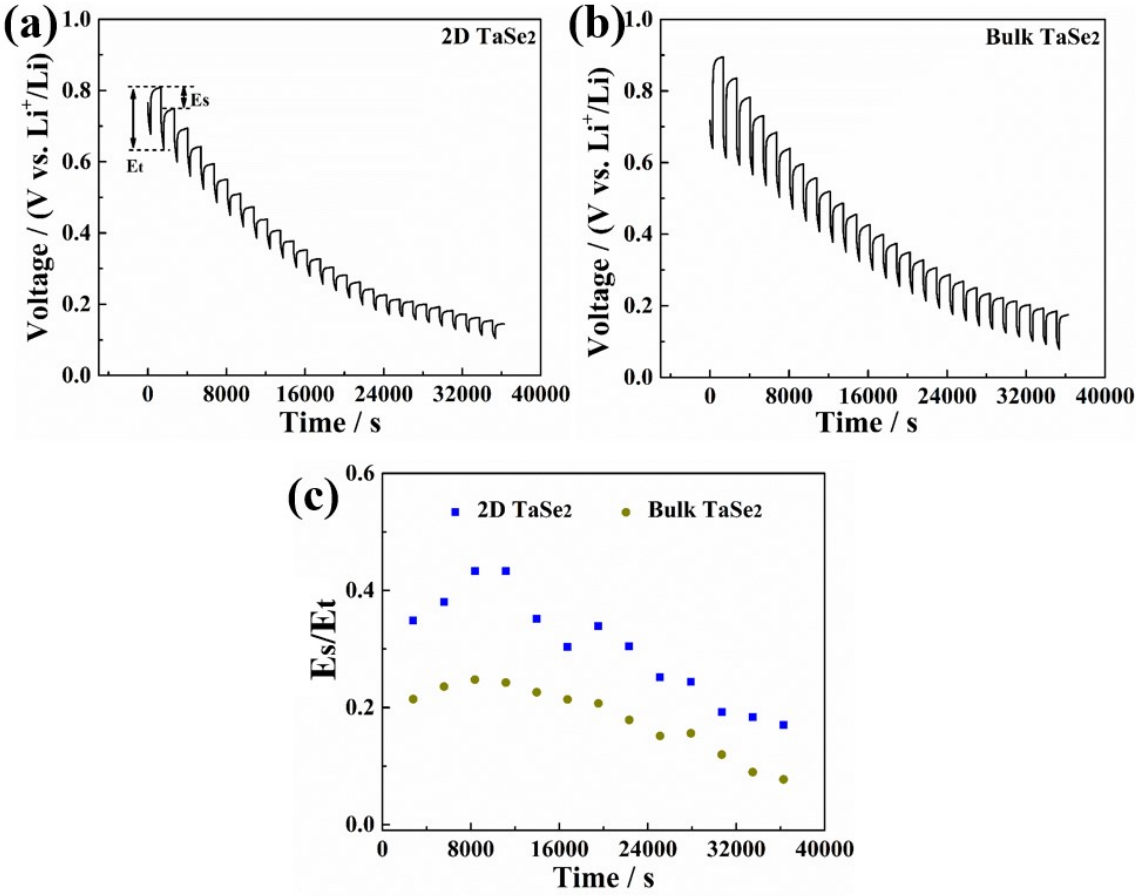

Figure S10. GITT curves of **(a)** 2D $TaSe_2$ and **(b)** bulk $TaSe_2$. **(c)** E_s/E_t values of the two electrodes.

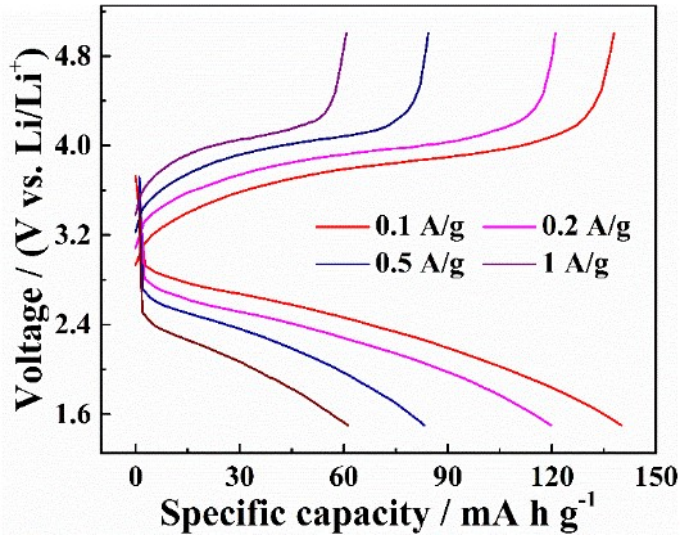

Figure S11. Discharge-charge curves of $LiFePO_4$||2D $TaSe_2$ full cell.

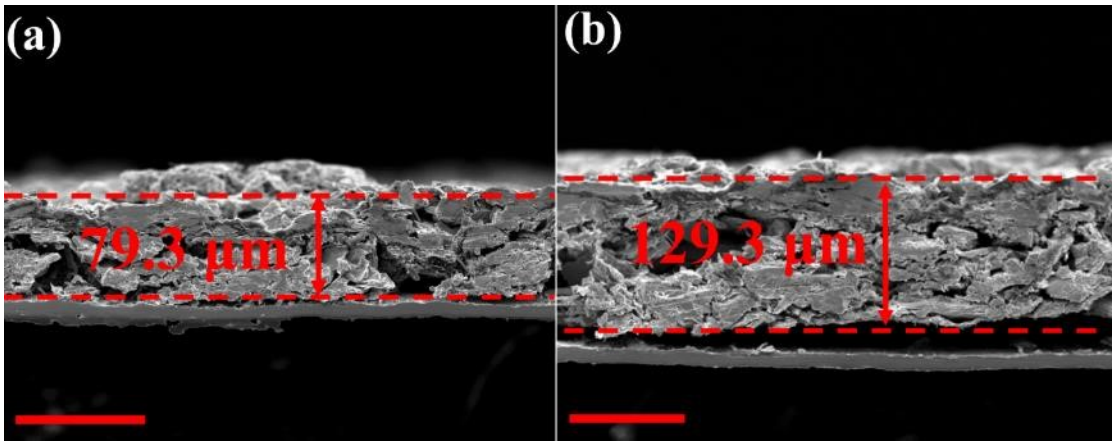

Figure S12. Electrodes thickness of ultrathick **(a)** bulk $TaSe_2$ and **(b)** 2D $TaSe_2$ electrodes (the scale bar is 100 μm) at full lithiation.

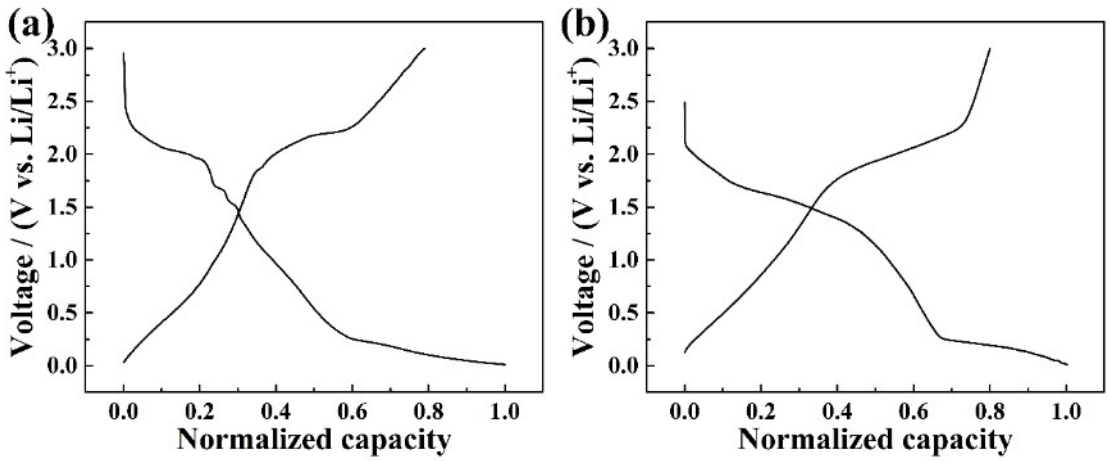

Figure S13. Discharge-charge curves of **(a)** 2D $TaSe_2$ and **(b)** bulk $TaSe_2$ anodes during in-situ XRD tests.

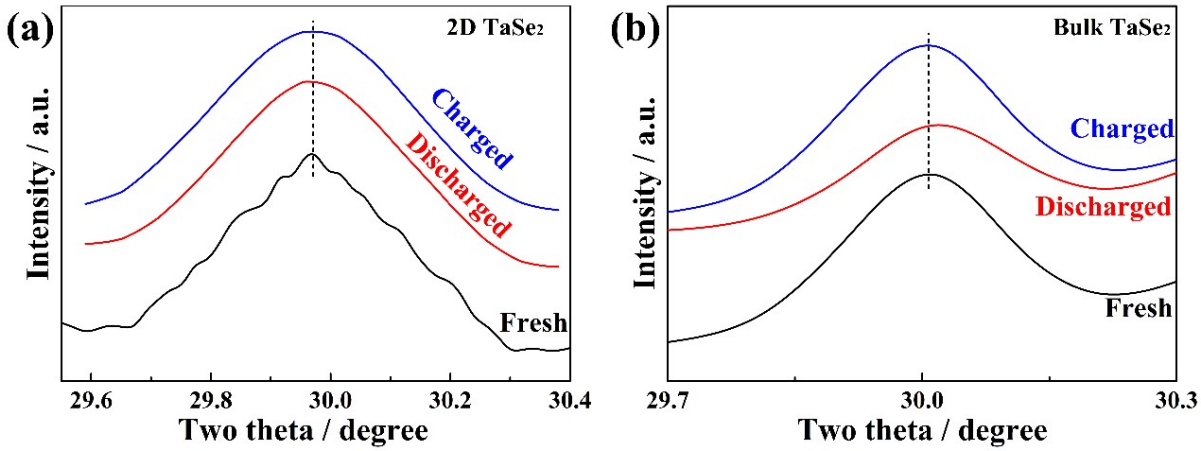

Figure S14. Enlarged in-situ XRD peaks of **(a)** 2D $TaSe_2$ and **(b)** bulk $TaSe_2$ for (100) plane.

Figure S15. Photograph of electrodes at full lithiation immersed in alcohol. Before immersing the electrode in alcohol, the electrode was washed with N-methyl pyrrolidone several times to remove the electrolyte.

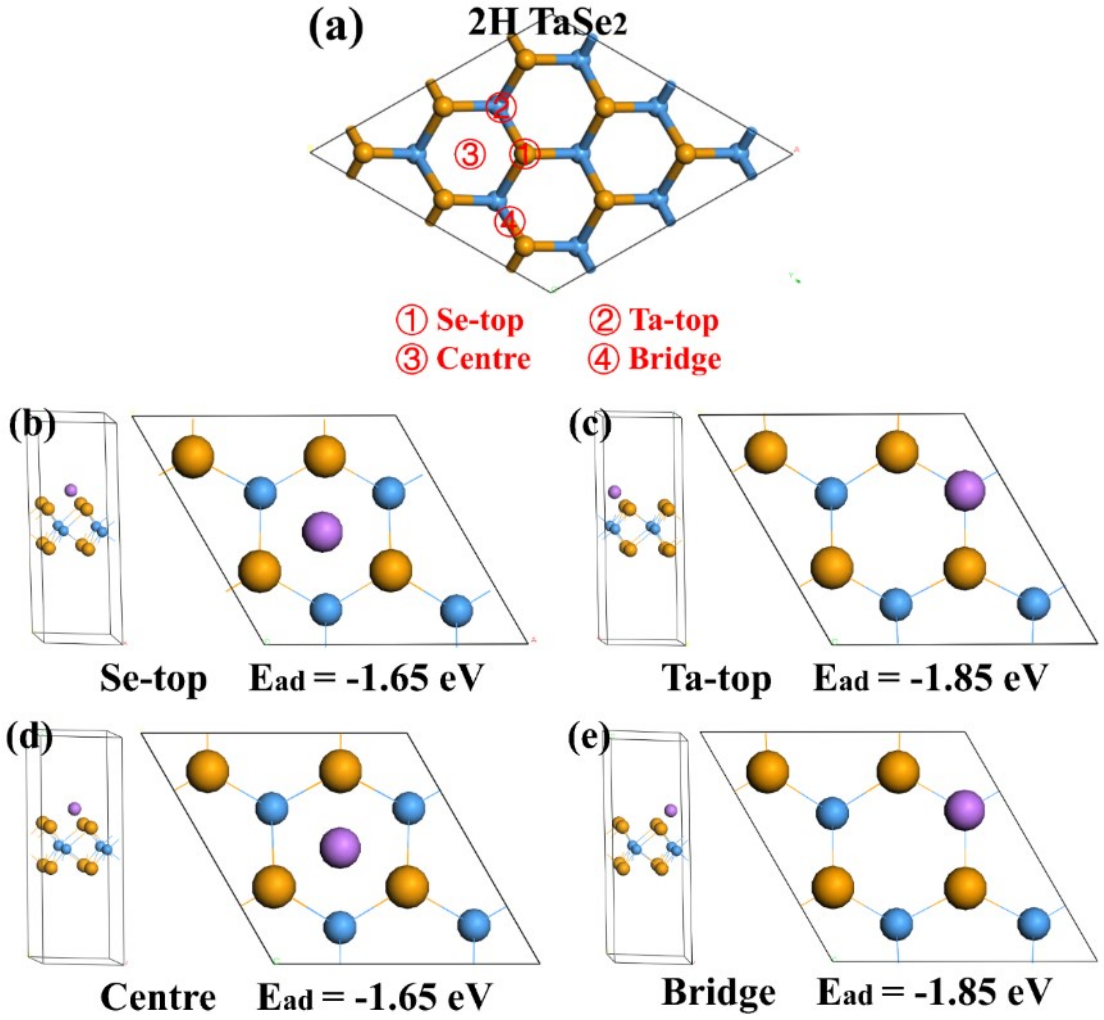

Figure S16. **(a)** Li^+ initial adsorbed sites on single layer 2H phase $TaSe_2$. Li^+ adsorption on single layer 2H phase $TaSe_2$ at initial **(b)** Se top, **(c)** Ta top, **(d)** centre and **(e)** bridge positions after structural optimization. The purple balls are Li atoms.

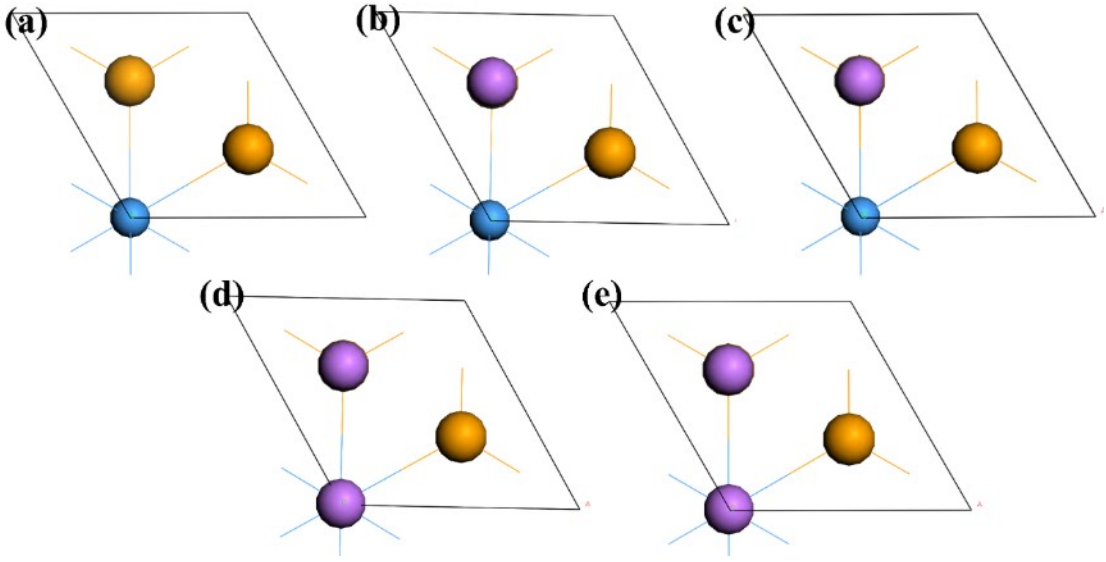

Figure S17. Top view of bulk Li_xTaSe_2 (**(a)** x=0, **(b)** x=1, **(c)** x=2 and **(d)** x=3 and **(e)** x=4).

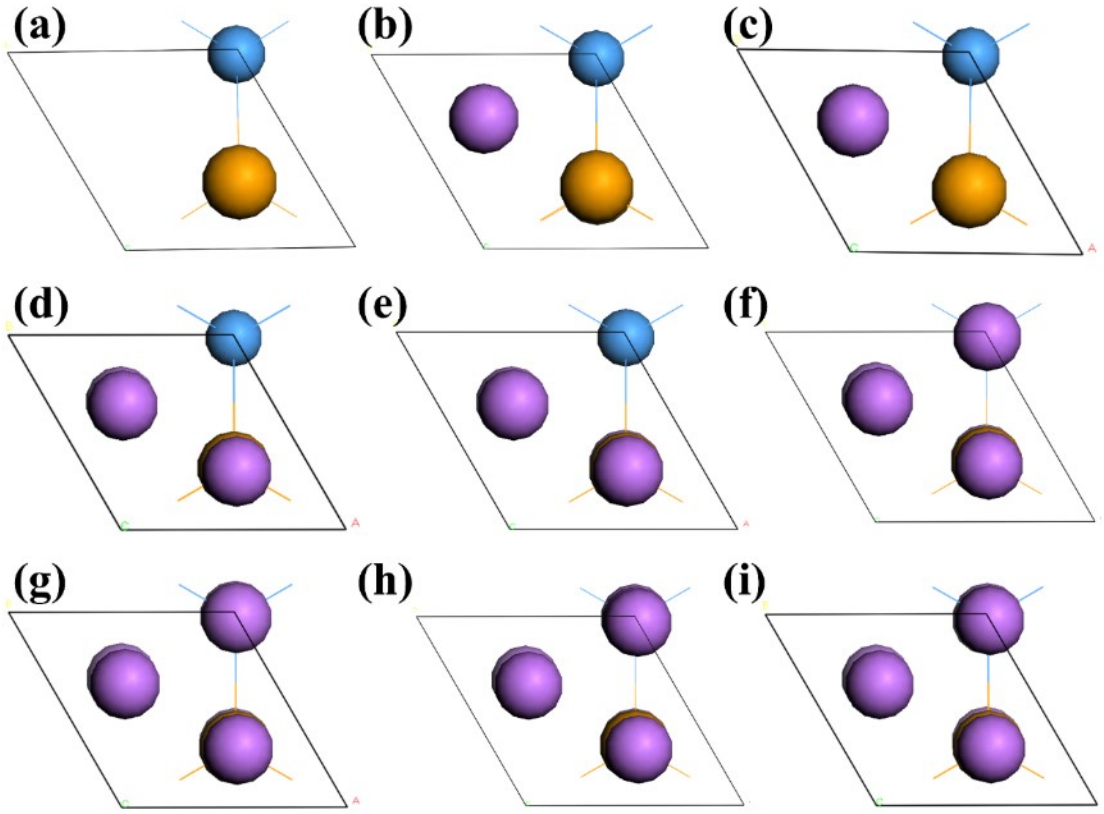

Figure S18. Top view of 2D Li_xTaSe_2 (**(a)** x=0, **(b)** x=1, **(c)** x=2 and **(d)** x=3 and **(e)** x=4, **(f)** x=5, **(g)** x=6, **(h)** x=7 and **(i)** x=8).

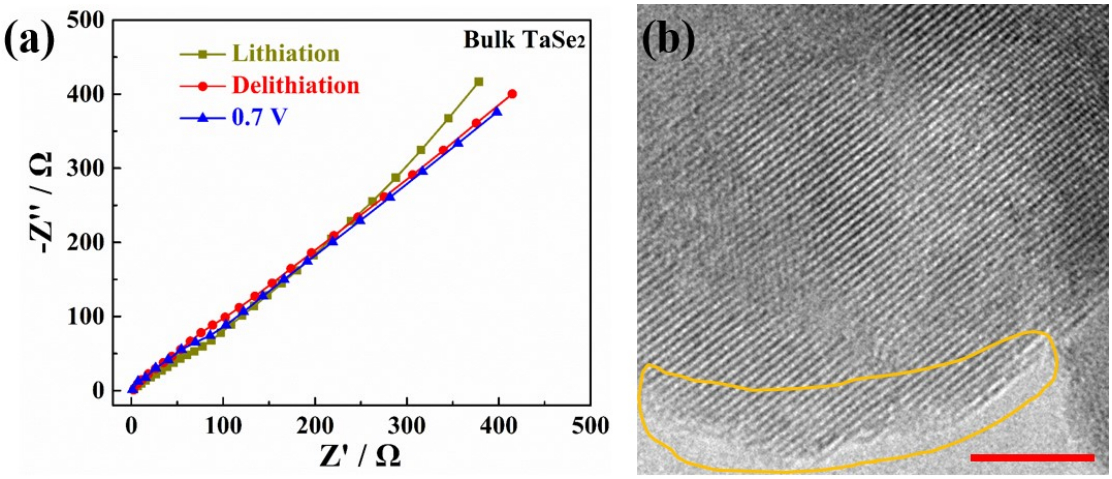

Figure S19. **(a)** EIS plots of bulk $TaSe_2$ at various states. (b) TEM morphology of 2D $TaSe_2$ at 3 V (the scale bar: 5 nm).

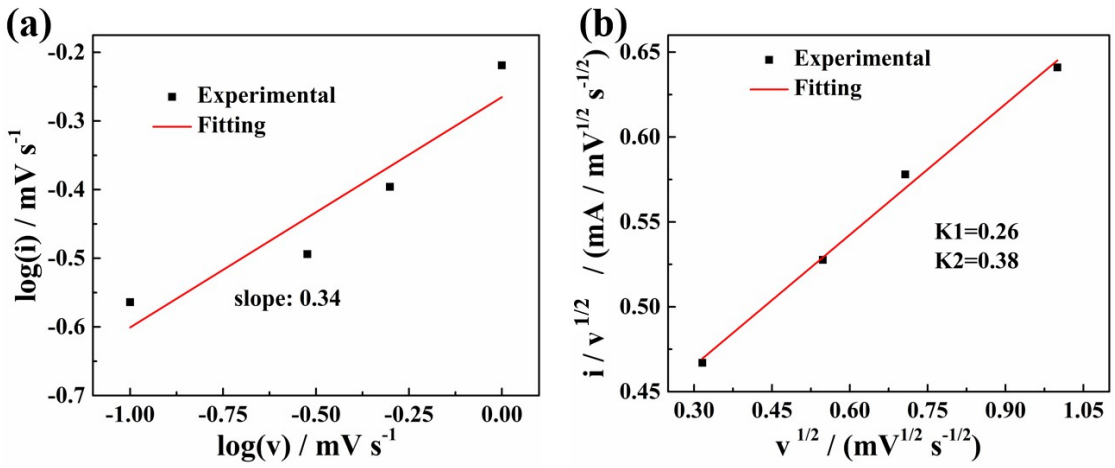

Figure S20. **(a)** log(i) *vs.* log(υ) curve and **(b)** ($i/\upsilon^{1/2}$) *vs.* $\upsilon^{1/2}$ curve for bulk $TaSe_2$.

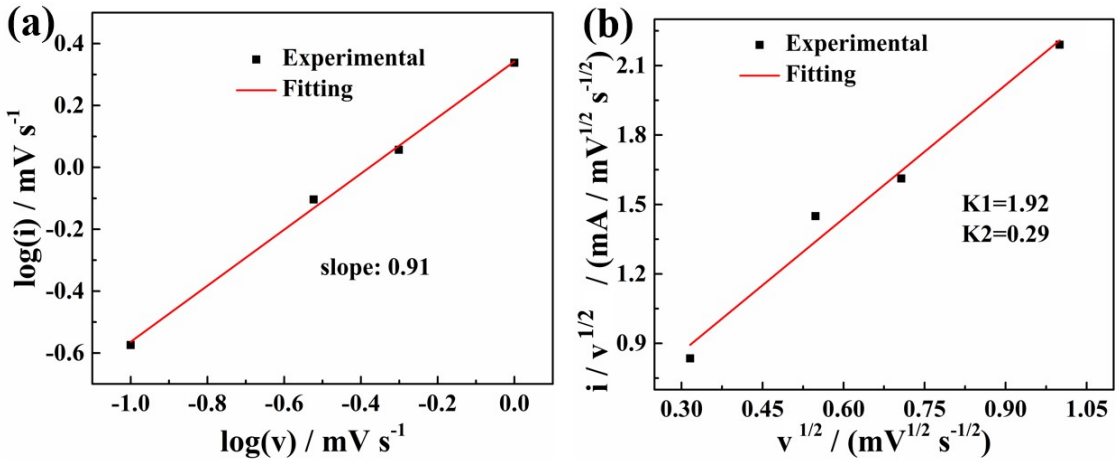

Figure S21. **(a)** log(i) *vs.* log(υ) curve and **(b)** ($i/\upsilon^{1/2}$) *vs.* $\upsilon^{1/2}$ curve for 2D $TaSe_2$.

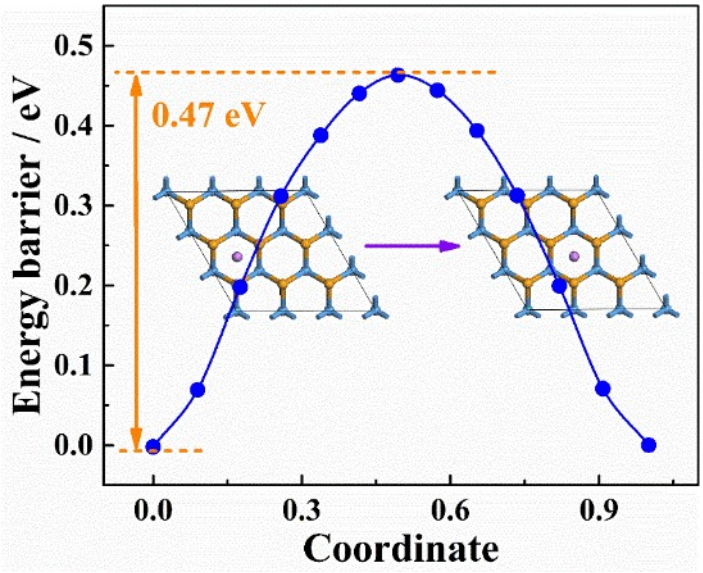

Figure S22. DFT calculations of Li^+ diffusion energy from centre to centre site.

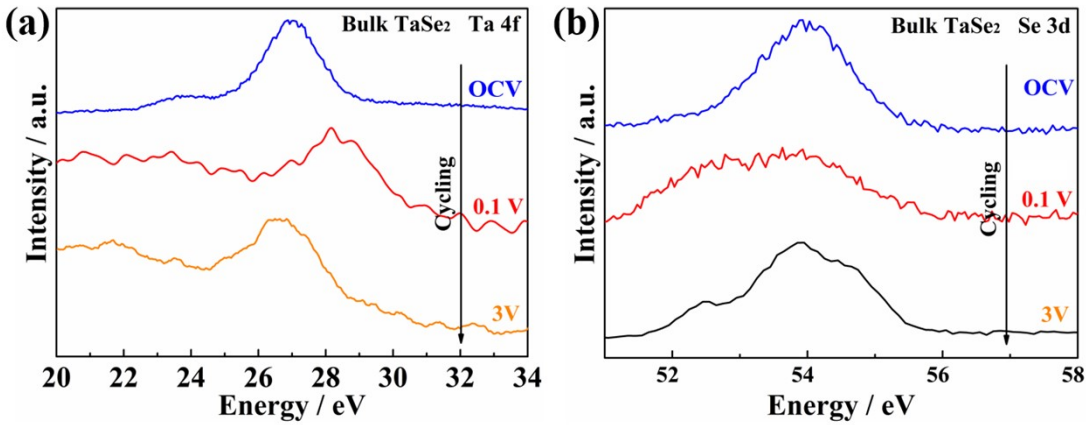

Figure S23. Ex-situ XPS **(a)** Ta 4f and **(b)** Se 3d spectra of 2D $TaSe_2$ anode during first cycle (0.1 and 3 V) and second cycle (3 V).

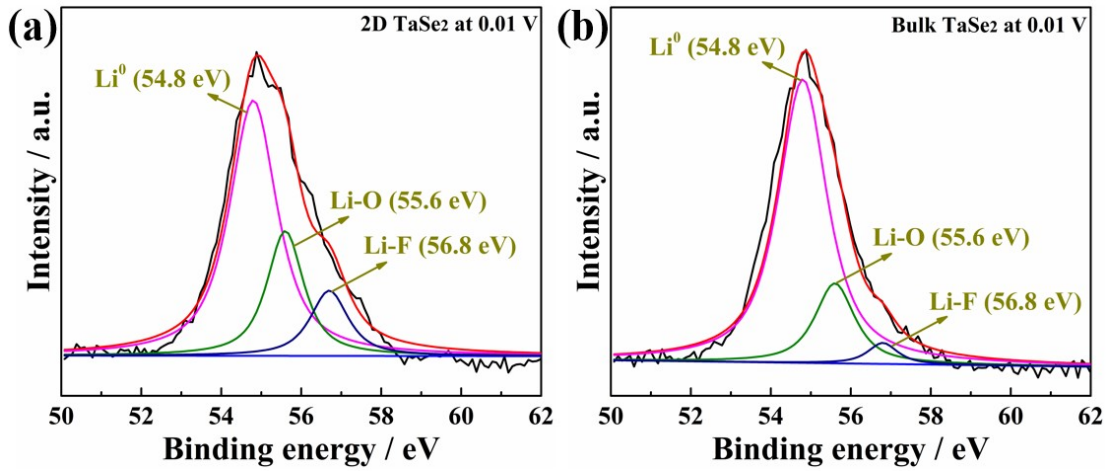

Figure S24. Ex-situ XPS Li 1s spectra of **(a)** 2D and **(b)** bulk $TaSe_2$ anode at 0.01 V.

Table S1. Young's modulus of $TaSe_2$ along various directions.

Direction	Young's modulus / GPa
a-axis	140.54
b-axis	140.54
c-axis	13.56

Table S2. Energy of a Li^+ on single layer 2H phase $TaSe_2$ with different configurations.

Configurations	Energy / eV
Se-top	-61346.2044
Ta-top	-61346.2822
Centre	-61346.2046
Bridge	-61346.2812
Slab without Li^+	-61142.1083

Table S3. Li/Ta mole ratio in Li_xTaSe_2 samples tests by the ICP-OES.

Sample	Li/Ta (lithiation)	Li/Ta (delithiation)
Bulk $TaSe_2$	4.14	0.067
2D $TaSe_2$	10.58	0.19

Table S4. Energy of bulk Li_xTaSe_2.

Number of Li^+	Energy / eV
0	-30571.5847
1	-30979.9961
2	-31385.7796
3	-31791.041
4	-32196.0252

Table S5. Energy of 2D Li_xTaSe_2.

Number of Li^+	Energy / eV
0	-15285.5181
1	-15489.8775
2	-15693.5445
3	-15896.8010
4	-16099.8376
5	-16302.6654
6	-16505.3248
7	-16707.8567
8	-16910.2312

Table S6. Li^+ diffusion energy in reported anode materials.

Anode materials	Energy barrier / eV	Ref.
Spinel $LiTi_2O_4$	~0.55 eV	[4]
$SrVO_3$	~0.80 eV	[5]
Lithium yttrium titanate	~0.23 eV	[6]
High-entropy transition- metal oxide	~0.83 eV	[7]
$Li_{3+x}V_2O_5$	~0.40 eV	[8]
MgB_2	~0.61 eV	[9]
BeB_2	~0.47 eV	[9]
2D-boron sheets	~0.62 eV	[10]
2D black arsenic	~0.18 eV	[11]
Graphdiyne	~0.30 eV	[12]
2D $TaSe_2$	~0.29 eV	This work
2D $TaSe_2$	~0.12 eV	This work

References

[1] Gao X, Zhang G, Luo L, et al. The effects of Ti and Cr on binding and diffusion of Al in V alloys: A first-principles study[J]. Computational Materials Science, 2018, 154: 8-13.
[2] Li Z, Liu B, Wang J, et al. Mechanism of intrinsic point defects and oxygen diffusion in yttrium aluminum garnet: first-principles investigation[J]. Journal of the American Ceramic Society, 2012, 95(11): 3628-3633.
[3] Zhang J , Zhang Y F , Li Y , et al. Blue-AsP monolayer as a promising anode material for lithium- and sodium-ion batteries: a DFT study[J]. Physical Chemistry Chemical Physics, 2021, 23, 5143.
[4] Wang Q, Yu H T, Xie Y, et al. Structural stabilities, surface morphologies and electronic properties of spinel LiTi2O4 as anode materials for lithium-ion battery: A first-principles investigation[J]. Journal of Power Sources, 2016, 319: 185-194.
[5] Li X, Lin Z, Jin N, et al. Perovskite-Type SrVO3 as High-Performance Anode Materials for Lithium-Ion Batteries[J]. Advanced Materials, 2021: 2107262.
[6] Zhang Y, Huang J, Saito N, et al. Layered Perovskite Lithium Yttrium Titanate as a Low-Potential and Ultrahigh-Rate Anode for Lithium-Ion Batteries[J]. Advanced Energy Materials, 2022: 2200922.
[7] Yang X, Wang H, Song Y, et al. Low-Temperature Synthesis of a Porous High-Entropy Transition-Metal Oxide as an Anode for High-Performance Lithium-Ion Batteries[J]. ACS Applied Materials & Interfaces, 2022, 14(23): 26873-26881.
[8] Liu H, Zhu Z, Yan Q, et al. A disordered rock salt anode for fast-charging lithium-ion batteries[J]. Nature, 2020, 585(7823): 63-67.
[9] Wan M, Zhao S, Zhang Z, et al. Two-Dimensional BeB_2 and MgB_2 as High Capacity Dirac Anodes for Li-Ion Batteries: A DFT Study[J]. The Journal of Physical Chemistry C, 2022, 126, 9642-9651.
[10] Banerjee S, Periyasamy G, Pati S K. Possible application of 2D-boron sheets as anode material in lithium ion battery: A DFT and AIMD study[J]. Journal of Materials Chemistry A, 2014, 2(11): 3856-3864.
[11] Akgenç B. Two-dimensional black arsenic for Li-ion battery applications: a DFT study[J]. Journal of Materials Science, 2019, 54(13): 9543-9552.
[12] Sun C, Searles D J. Lithium storage on graphdiyne predicted by DFT calculations[J]. The Journal of Physical Chemistry C, 2012, 116(50): 26222-26226.